Paper:

A Novel Visual-Inertial Navigation System with Yawing Constraints

JingZhe Wang, LeiLei Li, XunYa Gui, ZuCheng Li, YiXiang Wang

Beijing Institute of Technology
Beijing, China
E-mail: weskerredfield@aliyun.com, lileilei@bit.edu.cn, guixunya@hotmail.com, 469805550@qq.com, 13011101566@163.com
[Received 00/00/00; accepted 00/00/00]

Recent years have witnessed the rapid development of Visual-Inertial SLAM amid numerous theories and implementations ever emerging. Notwithstanding VI-SLAM's high accuracy and low computational cost, its yawing angle is still unobservable all the same, from which it follows that not only is its heading estimation drifts with time but its overall trajectory is bound to deviate, and therein lies the motivation of this paper. We propose a novel Visual-Inertial-Magnetic navigation system comprising an efficient initialization procedure capable of recovering IMU biases, the scalar factor of monocular vision, and the vectors of gravity and Magnetic North; a non-linear optimization module taking visual-inertial-magnetic information as observation. The system has been examined and evaluated on several datasets collected in large-scale outdoor environments. Analysis and comparisons validate its superiority in accuracy over VI-SLAM.

Keywords: Visual-Inertial SLAM, Visual-Inertial-Magnetic Information, non-linear optimization, heading estimation

1. INTRODUCTION

Visual-Inertial SLAM has been on its way towards maturation and perfection with numerous schemes ever coming up [1–3] in parallel with various applications [4, 5]. Fusion of visual and inertial information renders the angles of pitch and roll observable, and is therefore capable of elevating the precision of navigation in theory [6–8]. Be that as it may, the still unobservable yawing angle keeps derogating from the performance by making the estimated trajectory deviate. It stands to reason that if the yawing angle is better estimated, the overall accuracy will be enhanced in large measure. One type of sensors able to obtain heading information is the magnetometer that, as its name suggests, measures magnetic density in a magnetic field [9], especially the Earth's magnetic field (EMF) [10]. It has been employed in a wide range of commercial and military applications, usually in tandem with other types of apparatus such as an IMU and mostly for directional information [11]. Its application in SLAM and relevant research have yet to be done since it's rarely, if ever, been adopted in SLAM systems as a device to arrest accretion in yawing estimation, which leads to our attempt at presenting a novel Visual-Inertial-Magnetic navigation system built on and beyond VI-SLAM. This paper claims to have the following contributions:

- Elaborate mathematical deduction has been made to back up the proposed system theoretically, including the observation models of the three types of sensors, least squares problems concerned with initialization, and a novel optimization framework that fuses visual-inertial-magnetic information;
- A complete and reliable procedure of initialization for visual-inertial-magnetic navigation systems is presented;
- An effective and efficient optimization module taking visual-inertial-magnetic measurements as observation is built on ordinary VI-SLAM optimization;
- A suite of sensors and a CPU with other equipment, excellent in data acquisition and real-time operation, has been designed and assembled.
- The system has been tried and tested on several datasets recorded in large-scale outdoor environments. Analysis and comparisons of the experiment results testify to the viability, validity, and superiority of the proposed system.

2. RELATED WORK

Visual-Inertial navigation has been gaining in popularity in the robotic field. Much research has been done focusing on visual-inertial odometry (VIO) [12–14] and visual-inertial SLAM [4, 15, 16] either

by filtering [17] or based on non-linear optimization [4, 16].

Algorithms and implementations are as diverse as their application scenarios vary. Early schemes rest on various kinds of filters to estimate such as the extended Kalman filter (EKF) [12, 13, 18–20] and the unscented Kalman filter (UKF) [21–23]. As efficient and effective as they seem, filters are by definition unable to sustain consistency, which restricts their accuracy. Being more competent to maintain consistency, the incremental smoother [24, 25] and graph optimization [4, 26–28] are in the ascendant. What differentiates them from filters is that, rather than focusing only on the current state, they adjust the whole trajectory (or rather a certain length of it in most cases) every time a new measurement arrives.

Most navigation systems involving magnetometers fuse inertial and magnetic measurements [9, 29]. [30] presents a pose estimation method using visual, inertial and magnetic measurements, but magnetic information is exploited for velocity observation, rather than for heading reference.

Fig. 1. : The vehicle used for carrying sensors.

Fig. 2. : The device we use for data acquisition.

3. SYSTEM OVERVIEW

We adopt the following symbols throughout this paper. $(.)_W$ denotes the world frame, $(.)_{B_k}$ the k^{th} body frame which doubles as the k^{th} IMU frame as aligned with the body frame, $(.)_{C_k}$ the k^{th} camera frame, and $(.)_{M_k}$ the k^{th} magnetometer frame. As for measurements, w_k represents the gyroscope?s readings, a_k the accelerometer?s, and h_k the magnetometer?s, at k^{th} frame. $(u, v)_k$ the coordinates of a feature point in the k^{th} image.

The overall states to be estimated are expressed in such a vector as $x = \left[P, q, V, bg, ba, q_{BC}\right]_{B_k}$ with P the position, q the body orientation quaternion, V the velocity, b_g and b_a the gyroscope?s and accelerometer?s biases respectively at the k^{th} frame, q_{BC} the transformation from frame C to frame B intrinsic to the installation and thus considered to be invariant. L_W symbolizes a landmark expressed homogeneously with $L_W = \left[x, y, z, 1\right]$.

The proposed scheme depicted in fig 3 receives visual-inertial-magnetic information at different rates. It commences with initializing the system, after which it goes into the normal operation of alternating between prediction and optimization. Occasionally, a detected and verified loop closure triggers pose graph adjustment to ensure global consistency.

4. VISUAL-INERTIAL-MAGNETIC INITIALIZATION

For VI-SLAM or variants thereon, the initialization is as vital as it is demanding. How well it is initialized plays a huge part in whether or not it can function normally. A single wrongly estimated parameter could have repercussions for the entire system. This section lays out an efficient initialization procedure illustrated in fig 4 dedicated to Visual-Inertial-Magnetic SLAM.

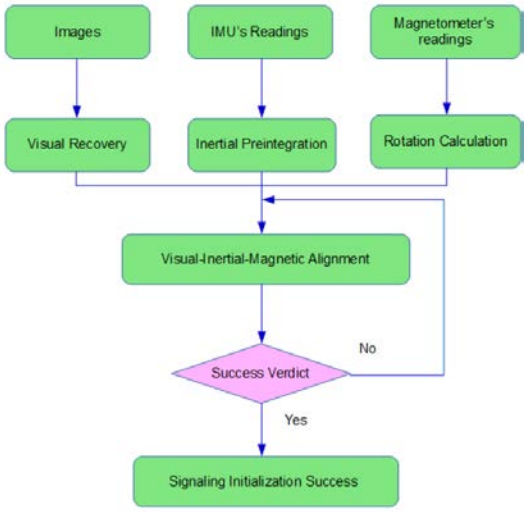

Fig. 4. : The flowchart of Visual-Inertial-Magnetic initialization

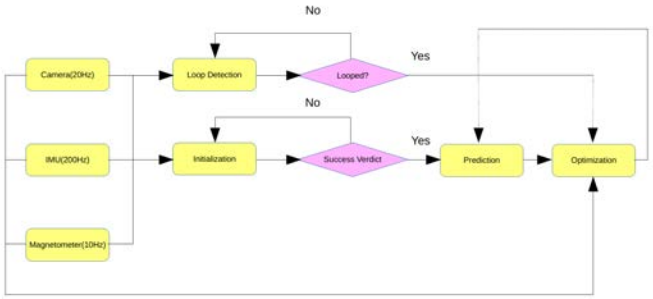

Fig. 3. : System Structure Overview

4.1. Visual recovery

What the visual module undertakes is to calculate the relative transformations between contiguous frames up to a scalar factor. It extracts the essential and homography matrices between two images with enough parallax and adopts one of them to decompose to recover the relative pose according to whose re-projection error is smaller, because not only translation but rotation alone effects parallax. The essential matrix is better at recovering poses with enough translation while the homography matrix is more appropriate for pure rotation situations. If there's enough translation between two images, the key points in them are triangulated and assigned depths. Following triangulation, all the intervening frames' poses are recovered using PnP (Perspective-n-Point) [31] with recourse to BA (Bundle Adjustment) [32].

4.2. Visual-Inertial-Magnetic alignment

Gyroscope biases are estimated by associating its preintegration with relative rotations to form (1).

$$\begin{aligned} &\Delta R_{B_k B_{k+1}} R(\frac{\partial \Delta R_{B_k B_{k+1}}}{\partial b_{w_{B_k}}} b_{w_{B_k}}) \\ &= R_{WC_k}^T R_{BC}^T R_{WC_{k+1}} R_{BC}^T \end{aligned} \tag{1}$$

where $\Delta R_{B_k B_{k+1}}$ is the rotational part of preintegration and $\frac{\partial \Delta R_{B_k B_{k+1}}}{\partial b_{w_{B_k}}}$ is its partial derivative with respect to gyroscope biases.

Preintegraion is recalculated with newly estimated biases. With the corrected preintegration, the scalar factor, the direction of gravity, and velocities can be worked out by combining visual and inertial estimation as (2) does.

$$\begin{aligned} {}^{\Delta}P^{B_k B_{k+1}} &= R_{WB_k}^T \mathbf{s} R_C^B P_W^{WC_{k+1}} \\ &\quad - R_{WB_k}^T (\mathbf{s} R_C^B P_W^{WC_k} + \Delta t \mathbf{V_W^{WB_k}} - \frac{1}{2} \Delta t^2 \mathbf{G_W}) \end{aligned} \tag{2a}$$

$$\begin{aligned} {}^{\Delta}V^{B_k B_{k+1}} &= R_{WB_k}^T \mathbf{V_W^{WB_{k+1}}} \\ &\quad - R_{WB_k}^T (\mathbf{V_W^{WB_k}} - \Delta t \mathbf{G_W}) \end{aligned} \tag{2b}$$

(2) resolves the problem of aligning the world frame with gravity, scaling up to real size, and estimating velocities, which is what the initialization essentially does for a typical VI-SLAM system. For VIMO, an extra step is to align the world frame yet again with EMF by rotating x-axis to be parallel to the vector of Magnetic North.

4.3. Initialization completion verdict

The results from the initialization module might be spurious in the wake of such rare but possible situations as moving at a constant speed and therefore certain measures need to be taken to collate its results.

Echoing [33] to a degree, the system reviews the estimation error of initialization which ties in with its uncertainty to determine whether it is initialized successfully.

5. NON-LINEAR OPTIMIZATION

For optimization, we use perturbations as increments to adjust variables as (3) shows.

$$T \leftarrow \delta T \otimes T \begin{cases} R \leftarrow \delta \mathbf{R} \cdot R \\ P \leftarrow P + \delta P \end{cases} \tag{3}$$

The optimization module is guided by three constraints, namely visual, inertial and magnetic constraints, and each thereof is established according to its observation model. Together they form an overall objective function that is to be minimized.

5.1. Visual constraint

The visual constraint is basically in line with reprojection error in the form of (4), which more or less bears a resemblance to [4, 33, 34].

$$E(i,k) = Z_k^i - \pi(\mathbf{T_{BC}}^T \mathbf{T_{WB}}^T \mathbf{L_W^{WL^i}}) \tag{4}$$

where i is the index of the ith landmark and k denotes the kth frame. $\pi(.)$ is the projection function characteristic of the camera used. T_{BC} is the transformation from f_C to f_B that ought to be constant given that the sensors are rigidly assembled. Variables to be optimized are in bold type.

The jacobians of the reprojection error with respect to each variable are as follows:

$$\begin{aligned}
\frac{\partial E(i,k)}{\partial R_{BC}} &= -R_{BC}^T(T_{WB}^T L_W^{WL^i} - t_{BC})^\times \\
\frac{\partial E(i,k)}{\partial t_{BC}} &= R_{BC}^T \\
\frac{\partial E(i,k)}{\partial R_{WB}} &= -R_{BC}^T R_{WB}^T (L_W^{WL^i} - t_{WB})^\times \\
\frac{\partial E(i,k)}{\partial t_{WB}} &= R_{BC}^T R_{WB}^T
\end{aligned}$$

where t_{BC} and t_{WB} are the translation parts of T_{BC} and T_{WB}. The above jacobians are deduced with rotation and translation variables treated separately as they are when being updated, rather than manipulated as a whole as in [35].

5.2. Inertial constraint

(5) is the observation model of the IMU that is based on the technique of pre-integration on manifold first proposed in [26, 36].

$$\begin{aligned}
{}^{\Delta}P^{B_kB_{k+1}} =& {\mathbf{R_{WB_k}}}^T \mathbf{P_W^{WB_{k+1}}} \\
& - \mathbf{R_{WB_k}}^T(\mathbf{P_W^{WB_k}} + \Delta t \mathbf{V_W^{WB_k}} - \tfrac{1}{2}\Delta t^2 G_W) && (5a)\\
{}^{\Delta}V^{B_kB_{k+1}} =& \mathbf{R_{WB_k}}^T \mathbf{V_W^{WB_{k+1}}} - \mathbf{R_{WB_k}}^T(\mathbf{V_W^{WB_k}} - \Delta t G_W) && (5b)\\
{}^{\Delta}R^{B_kB_{k+1}} =& \mathbf{R_{WB_k}}^T \mathbf{R_{WB_{k+1}}} && (5c)
\end{aligned}$$

According to inertial observation model, its cost functions are established as (6) whose deduction details are adequately presented in [28, 33]

$$\begin{aligned}
\mathfrak{R}_{inertia} &= \begin{bmatrix} \mathfrak{R}_{B_kB_{k+1}}(P) \\ \mathfrak{R}_{B_kB_{k+1}}(V) \\ \mathfrak{R}_{B_kB_{k+1}}(\theta) \\ \mathfrak{R}_{B_kB_{k+1}}(b_w) \\ \mathfrak{R}_{B_kB_{k+1}}(a_w) \end{bmatrix} \\
&= \begin{bmatrix} {}^{\Delta}P^{B_kB_{k+1}} - \mathbf{R_{WB_k}}^T(\mathbf{P_W^{WB_{k+1}}} - \mathbf{P_W^{WB_k}} - \Delta t \mathbf{V_W^{WB_k}} + \frac{1}{2}\Delta t^2 G_W) \\ {}^{\Delta}V^{B_kB_{k+1}} - \mathbf{R_{WB_k}}^T(\mathbf{V_W^{WB_{k+1}}} - \mathbf{V_W^{WB_k}} + \Delta t G_W) \\ {}^{\Delta}R_{B_kB_{k+1}}^T \oplus \mathbf{R_{WB_k}}^T \mathbf{R_{WB_{k+1}}} \\ \mathbf{b_{w_{B_{k+1}}}} - \mathbf{b_{w_{B_k}}} \\ \mathbf{b_{a_{B_{k+1}}}} - \mathbf{b_{a_{B_k}}} \end{bmatrix}
\end{aligned} \quad (6)$$

5.3. Magnetic constraint

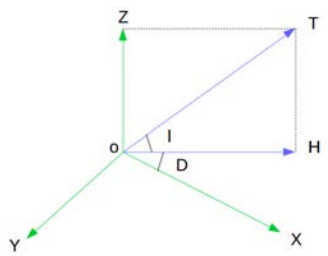

Fig. 5. : The Geomagnetic and Geographic coordinate frames

In fig 5:

- **T** – the vector of the total density EMF;
- **X**, **Y** ,and **Z** – the Geographic System Coordinates;
- **I** – the angle of magnetic inclination;
- **D** – the angle of magnetic declination;

T, **I**, **D** can be determined by consulting geomagnetic maps.

The magnetometer's calibration model is

$$\begin{bmatrix} M_{xt} \\ M_{y_t} \\ M_{zt} \end{bmatrix} = \begin{bmatrix} k_{xx} & k_{yx} & k_{zx} \\ k_{yy} & k_{xy} & k_{zy} \\ k_{zz} & k_{xz} & k_{yz} \end{bmatrix} \begin{bmatrix} M_x \\ M_y \\ M_z \end{bmatrix} - \begin{bmatrix} b_{m_x} \\ b_{m_y} \\ b_{m_z} \end{bmatrix}$$

where: $\begin{bmatrix} M_x & M_y & M_z \end{bmatrix}^T$ is the magnetometer's readings that are a coefficient matrix and a bias vector away from the true projection on the sensor's body frame $\begin{bmatrix} M_{xt} & M_{y_t} & M_{zt} \end{bmatrix}^T$; k_{xx}, k_{yy}, and k_{zz} are scalar factor coefficients; k_{xy}, k_{yz}, and k_{zx} are the transverse coefficients caused by the magnetometer's axes non-orthogonality; b_{m_x}, b_{m_y}, and b_{m_z} are biases' correction coefficients in line with by local magnetic field.

According to fig 5, the observation model of the magnetometer is (7).

$$M_M = R_{MB} R_{WB}^T H_W \quad . \quad . \quad . \quad . \quad . \quad . \quad . \quad . \quad . \quad (7)$$

where R_{MB} is the relative rotation matrix from the body frame f_B to the magnetometer's frame f_M, and is determined through calibration.

Corresponding to (7), the Jacobians of the observation function with respect to the variable R_{WB} are (8)

$$J_{\frac{M}{R}} = \frac{\partial M_M}{\partial R_{WB}} = R_{MB} R_{WB}^T H_W^\times \quad . \quad . \quad . \quad . \quad . \quad (8)$$

6. EXPERIMENT RESULTS

The navigation system's software is programmed in C++ on Ubuntu 16.04. The work of programming is relieved of complicated data exchange by ROS (Robot Operating System) [37] and of the daunting task of implementing optimization by ceres-solver [37]. The system runs on a standard central processing unit (Intel® NUC Kit NUC7i7BNH, Intel® Core i7-7567U Processor, 16GB RAM).

In fig 6, the trajectories estimated by VI-SLAM and VIMO diverge after the vehicle takes a turning. For VI-SLAM, an error in yaw estimation causes the whole trajectory to go off course of the groundtruth, whereas for VIMO this issue is obviated by virtue of absolute heading reference from the magnetometer.

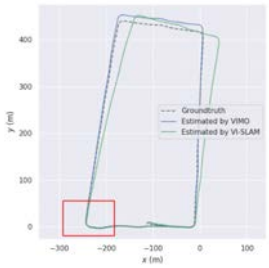

Fig. 6. : Trajectory Comparison

As figure 6 illustrates, the difference in accuracy between the two begins to build up after the vehicle corners, and the error in VI-SLAM's estimation continues growing larger while VIMO's remains nearly on the groundtruth.

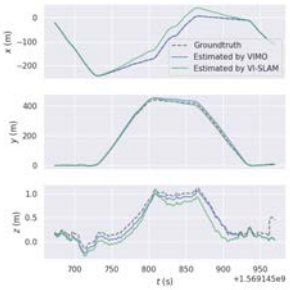

Fig. 7. : Trajectories Projected onto XYZ axes

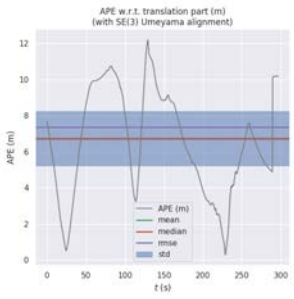

Fig. 8. : The Absolute Pose Error (APE), mean and median of errors, Root Mean Squared Error (RMSE), and Standard Deviation (STD) of VI-SLAM

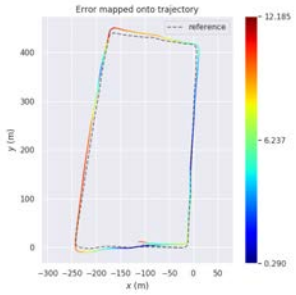

Fig. 9. : The Error Map of VI-SLAM

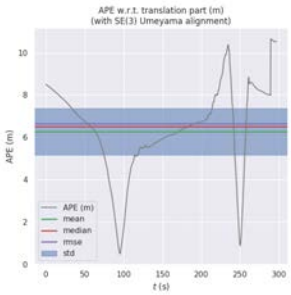

Fig. 10. : The Absolute Pose Error (APE), mean and median of errors, Root Mean Squared Error (RMSE), and Standard Deviation (STD) of VIMO

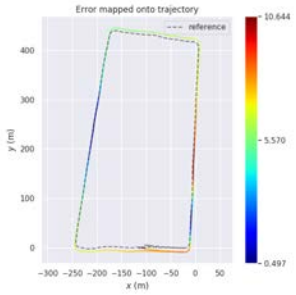

Fig. 11. : The Error Map of VIMO

Table 1. : Absolute Pose Errors (APEs) that include the maximal error (max), the mean error (mean), the median of all discrete errors (median), the minimal error (min), the root mean square error (rmse), the standard deviation of errors (std)

Error Terms	max	mean	median	rmse	std
VI-SLAM	12.1847	6.7346	6.7127	7.3614	2.9723
VIMO	10.6441	6.2678	6.5150	6.6390	2.1889

In table 1, the errors by VIMO (Max: 10.6441 m, Mean: 6.2678 m, Median: 6.5150 m, RMSE: 6.6390

m, StD: 2.1889 m) are lower than those by VI-SLAM (Max: 12.1847 m, Mean: 6.7346 m, Median: 6.7127 m, RMSE: 7.3614 m, StD: 2.9723 m) for all error items. This improvement in navigation precision is attributed to curbed yaw drift as evidenced in figs 6, 7, 8, 9, 10.

7. CONCLUSION

In this paper, we propose a novel Visual-Inertial-Magnetic navigation system comprising an efficient initialization procedure capable of recovering IMU biases, the scalar factor of monocular vision, and the vectors of gravity and Magnetic North; a non-linear optimization module taking visual-inertial-magnetic information as observation. In the end, we demonstrate the proposed system's superiority over common VI-SLAM through real world experiment,s along with result analysis and performance comparison.

References:

[1] Nam Dinh and Gon-Woo Kim. Robust stereo visual inertial navigation system based on multi-stage outlier removal in dynamic environments. *Sensors*, 20:2922, 05 2020.

[2] Michael Bloesch, Sammy Omari, Marco Hutter, and Roland Siegwart. Robust visual inertial odometry using a direct ekf-based approach. pages 298–304, 09 2015.

[3] Kyuman Lee and Eric Johnson. Latency compensated visual-inertial odometry for agile autonomous flight. *Sensors*, 20:2209, 04 2020.

[4] Stefan Leutenegger, Simon Lynen, Michael Bosse, Roland Siegwart, and Paul Furgale. Keyframe-based visual-inertial odometry using nonlinear optimization. *The International Journal of Robotics Research*, 34, 02 2014.

[5] Yonggen Ling, Tianbo Liu, and Shaojie Shen. Aggressive quadrotor flight using dense visual-inertial fusion. In *2016 IEEE International Conference on Robotics and Automation (ICRA)*, 2016.

[6] Joel Hesch, Dimitrios Kottas, Sean Bowman, and Stergios Roumeliotis. Camera-imu-based localization: Observability analysis and consistency improvement. *International Journal of Robotics Research*, 33:182–201, 01 2014.

[7] S. Tsao and S. Jan. Observability analysis and performance evaluation of ekf-based visual-inertial odometry with online intrinsic camera parameter calibration. *IEEE Sensors Journal*, 19(7):2695–2703, 2019.

[8] G. Panahandeh, M. Jansson, and P. Händel. Calibration of an imu-camera cluster using planar mirror reflection and its observability analysis. *IEEE Transactions on Instrumentation and Measurement*, 64(1):75–88, 2015.

[9] Felix Goldenberg. Geomagnetic navigation beyond the magnetic compass. *IEEE PLANS, Position, Location and Navigation Symposium*, 2006, 01 2006.

[10] R. Hilberg. The earth's magnetic field. 02 1967.

[11] Jingzhe Wang, Leilei Li, Huan Yu, Xunya Gui, and Zucheng Li. Vimo: A visual-inertial-magnetic navigation system based on non-linear optimization. *Sensors*, 20:4386, 08 2020.

[12] Anastasios I. Mourikis and Stergios I. Roumeliotis. A multi-state constraint kalman filter for vision-aided inertial navigation. In *IEEE International Conference on Robotics & Automation*, 2007.

[13] Zheng Huai and Guoquan Huang. Robocentric visual–inertial odometry. *The International Journal of Robotics Research*, page 027836491985336, 07 2019.

[14] Mingyang Li and Anastasios I. Mourikis. High-precision, consistent ekf-based visual-inertial odometry. *International Journal of Robotics Research*, 2013.

[15] Todd Lupton and Salah Sukkarieh. *Visual-Inertial-Aided Navigation for High-Dynamic Motion in Built Environments Without Initial Conditions*. IEEE Press, 2012.

[16] S. Shen, N. Michael, and V. Kumar. Tightly-coupled monocular visual-inertial fusion for autonomous flight of rotorcraft mavs. In *2015 IEEE International Conference on Robotics and Automation (ICRA)*, pages 5303–5310, 2015.

[17] Averil Chatfield. Fundamentals of high accuracy inertial navigation. 08 2020.

[18] Jonghyuk Kim and Salah Sukkarieh. Real-time implementation of airborne inertial-slam. *Robotics & Autonomous Systems*, 55(1):62–71, 2007.

[19] Mitch Bryson and Salah Sukkarieh. Observability analysis and active control for airborne slam. *IEEE Transactions on Aerospace & Electronic Systems*, 44(1):261–280, 2008.

[20] A. Mourikis, N. Trawny, S. Roumeliotis, A. Johnson, A. Ansar, and L. Matthies. Vision-aided inertial navigation for spacecraft entry, descent, and landing. *IEEE Transactions on Robotics*, 25(2):264–280, 2009.

[21] Sedat Ebcin and Michael Veth. Tightly-coupled image-aided inertial navigation using the unscented kalman filter. 01 2007.

[22] Giuseppe Loianno, Michael Watterson, and Vijay Kumar. Visual inertial odometry for quadrotors on se(3). In *2016 IEEE International Conference on Robotics and Automation (ICRA)*, 2016.

[23] Martin Brossard, Silvère Bonnabel, and Axel Barrau. Invariant kalman filtering for visual inertial slam. pages 2021–2028, 07 2018.

[24] Dennis Strelow. Motion estimation from image and inertial measurements. *The International Journal of Robotics Research*, 23:1157–1195, 12 2004.

[25] Vadim Indelman, Stephen Williams, Michael Kaess, and Frank Dellaert. Information fusion in navigation systems via factor graph based incremental smoothing. *Robotics & Autonomous Systems*, 61(8):721–738, 2013.

[26] Christian Forster, Luca Carlone, Frank Dellaert, and Davide Scaramuzza. On-manifold preintegration for real-time visual–inertial odometry. *ieee transactions on robotics*, 33(1):1–21, 2017.

[27] Kevin Eckenhoff, Patrick Geneva, and Guoquan Huang. Closed-form preintegration methods for graph-based visual–inertial navigation. *The International Journal of Robotics Research*, 38:027836491983502, 04 2019.

[28] Tong, Qin, Peiliang, Li, Shaojie, and Shen. Vins-mono: A robust and versatile monocular visual-inertial state estimator. *IEEE Transactions on Robotics*, 2018.

[29] Andrea Cereatti, Ugo Della Croce, and Angelo Sabatini. *Three-Dimensional Human Kinematic Estimation Using Magneto-Inertial Measurement Units*, pages 1–24. 04 2017.

[30] David Caruso, Alexandre Eudes, Martial Sanfourche, David Vissiere, and Guy Le Besnerais. An inverse square root filter for robust indoor/outdoor magneto-visual-inertial odometry. pages 1–8, 09 2017.

[31] Adrian Penate-Sanchez, Juan Andrade Cetto, and Francesc Moreno-Noguer. Exhaustive linearization for robust camera pose and focal length estimation. *IEEE transactions on pattern analysis and machine intelligence*, 01 2013.

[32] Bill Triggs, Philip Mclauchlan, and Richard Hartley. Bundle ajustment – a modern synthesis. 08 2000.

[33] Raul Mur-Artal and Juan Tardos. Visual-inertial monocular slam with map reuse. *IEEE Robotics and Automation Letters*, PP, 10 2016.

[34] Raul Mur-Artal, Jose Maria Martinez Montiel, and Juan D Tardos. Orb-slam: a versatile and accurate monocular slam system. *IEEE transactions on robotics*, 31(5):1147–1163, 2015.

[35] Ethan Eade. Lie groups for 2d and 3d transformations. *URL http://ethaneade. com/lie. pdf, revised Dec*, 117:118, 2013.

[36] Christian Forster, Luca Carlone, Frank Dellaert, and Davide Scaramuzza. Imu preintegration on manifold for efficient visual-inertial maximum-a-posteriori estimation. 07 2015.

[37] Morgan Quigley, Ken Conley, Brian Gerkey, Josh Faust, Tully Foote, Jeremy Leibs, Rob Wheeler, and Andrew Ng. Ros: an open-source robot operating system. volume 3, 01 2009.